A wide-field time-domain fluorescence lifetime imaging microscope with optical sectioning

S. E. D. Webb,[a] Y. Gu, S. Lévêque-Fort, J. Siegel, M. J. Cole, K. Dowling, R. Jones, and P. M. W. French
Femtosecond Optics Group, Department of Physics, Imperial College of Science, Technology and Medicine, Prince Consort Road, London SW7 2BW, United Kingdom

M. A. A. Neil, R. Juškaitis, L. O. D. Sucharov, and T. Wilson
Department of Engineering Science, University of Oxford, Parks Road, Oxford OX1 3PJ, United Kingdom

M. J. Lever
Department of Bioengineering, Imperial College of Science, Technology and Medicine, Exhibition Road, London SW7 2BX, United Kingdom

(Received 27 September 2001; accepted for publication 9 January 2002)

This article describes a wide-field time-domain fluorescence lifetime imaging (FLIM) microscope with optical sectioning. The FLIM system utilizes a wide-field time-gated optical image intensifier, with a minimum gate width of 85 ps, to achieve high temporal resolution of fluorescence decays induced by ultrashort laser pulses. Different configurations, using excitation pulses of picojoule energy at 80 MHz repetition rate and of nanojoule energy at 10 kHz, are compared. The instrument has a temporal dynamic range spanning from 100 ps to tens of μs and is shown to have a temporal discrimination better than 10 ps. When applied to laser dye samples, it has produced FLIM maps demonstrating sensitivity to variations in both chemical species and local environment, e.g., viscosity. Wide-field optical sectioning is achieved using the technique of structured illumination, which is applied to remove out-of-focus light that can result in lifetime artifacts. The sectioning strength, which may be adjusted by choosing an appropriate spatial modulation frequency, is characterized and shown to be comparable to that of a confocal microscope. Practical considerations concerned with improving the quality of sectioned fluorescence lifetime maps, including using a large bit depth camera, are discussed.
[DOI: 10.1063/1.1458061]

I. INTRODUCTION

Fluorescence microscopy is widely applied to biology and medicine as a means of imaging anatomical features and contrasting different chemical species (fluorophores) or different fluorophore microenvironments. Fluorescence radiation may be characterized in terms of its intensity, spectral, or temporal properties. Fluorescence contrast can be intrinsic, arising from autofluorescence of *endogenous* fluorophores, or it can be enhanced using an *exogenous* fluorophore that binds to specific features of interest. The contrast can be derived from the presence of specific fluorophores or from the perturbation to the fluorescence process caused by the local environment of fluorophore molecules. These are usually manifested through their impact on the radiative and nonradiative decay rates respectively.[1] The quantum efficiency of the fluorescence depends on both the radiative and nonradiative decay rates and so, in principle, it may be used to provide ''functional'' information. However, determination of the quantum efficiency from intensity measurements requires knowledge of the absolute intensities of the absorbed and emitted light and the fluorophore concentration, which can be made difficult by biological tissue heterogeneity (i.e., spatial variation of the fluorophore concentration and tissue optical properties) and strong scattering of optical radiation. Contrast can also be obtained from the fluorescence *lifetime*, however, which also depends on the radiative and nonradiative decay rates but which may be determined from relative measurements with no knowledge of the fluorophore concentration. It is thus often a more useful probe of fluorophore environment. Fluorescence lifetime probes have been demonstrated for many biochemically relevant indicators such as *p*H (Ref. 2) and $[Ca^{2+}]$.[3] In addition, the fluorescence lifetime may provide contrast between different fluorophores with indistinguishable fluorescence spectra, for example the major tissue constituents collagen, and elastin, at 415 nm excitation.[4] Fluorescence lifetime *imaging* (FLIM) using autofluorescence is particularly exciting since it offers the potential for noninvasive functional/diagnostic imaging. For many practical applications of FLIM, it is desirable to acquire fluorescence lifetime images as fast as possible. This suggests that wide-field FLIM with parallel image pixel acquisition is an appropriate approach. We describe here such a system that provides functional images with high temporal and spatial resolution in three dimensions.

Fluorescence lifetime imaging has been conducted in both the time domain[5] and the frequency domain.[6] In time-domain FLIM, a pulsed laser source is used for excitation

[a]Electronic mail: stephen.webb@ic.ac.uk

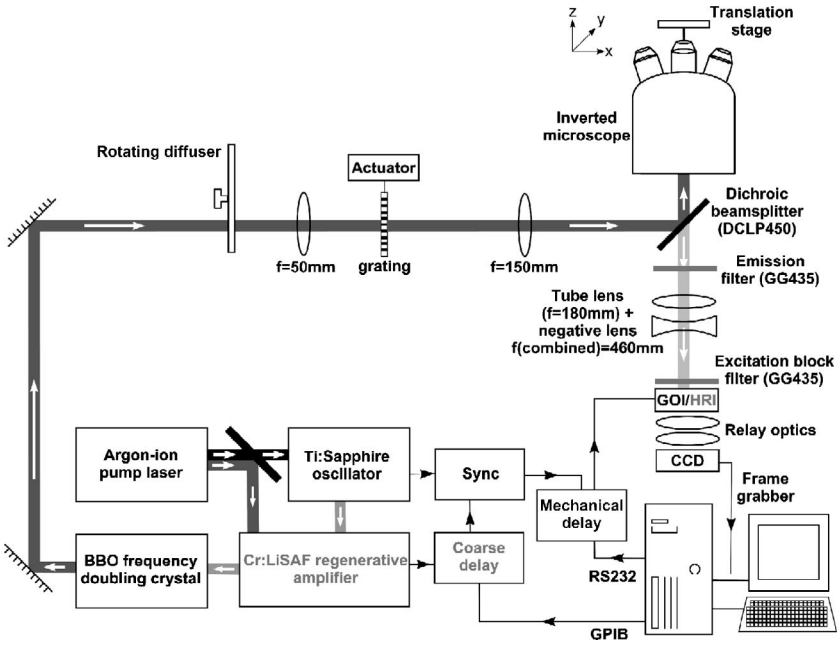

FIG. 1. FLIM microscope. The Cr:LiSAF regenerative amplifier and coarse delay may be eliminated and the Ti:sapphire oscillator pulses frequency doubled directly if the HRI is used instead of the GOI. The grating and actuator are required for optical sectioning by structured illumination.

and the fluorescence emission decay is sampled, using a time-gated detector, at various delays following the excitation pulse. For frequency-domain measurements, the intensity of a continuous wave laser excitation source is sinusoidally modulated and so generates a correspondingly modulated fluorescence emission. The lifetime may be calculated from the phase shift or the fall in modulation depth of the fluorescence signal relative to the excitation signal. Although the frequency-domain instrumentation is rather simpler to develop, time-domain FLIM systems are increasingly attractive due to their superior temporal resolution and the decreasing cost of ultrafast laser sources and gated optical intensifiers (GOIs). Time-domain systems yield a series of images of decreasing intensity that in itself gives an immediate qualitative indication of the fluorescence lifetimes present in the field of view and which is thus readily understandable to a scientist unfamiliar with FLIM technology. However, the data in a frequency-domain system are values for modulation change and phase shift, from which the temporal fluorescence decay parameters are calculated. Interpretation of such experimental data can become complicated and ambiguous when analyzing complex fluorescence decay profiles. In the time domain, the number of fluorescence decay components can be determined by finding the best fit to the acquired data *after* acquisition using, e.g., single or multiple discrete exponential components,[4] or a stretched exponential decay model.[7] In the frequency domain, it is necessary to make separate measurements for each component of a multiexponential decay,[8] requiring a prior assumption of the number of components, although it is possible to acquire these different frequency measurements in parallel.[9]

Optically sectioned FLIM is mostly implemented in confocal[10] or multiphoton[11] scanning microscopes. For many biomedical applications, it is critical to acquire fluorescence information with a minimum excitation intensity and in as short a time as possible, due to photobleaching or dynamic changes in the sample. Confocal and two-photon microscopes carry the disadvantage of sequential pixel-by-pixel scanning; although acquiring fluorescence of multiple pixels in parallel can help to reduce image acquisition times,[12] the detection efficiency is still inferior to wide-field techniques. Our optically sectioning FLIM microscope is truly wide-field and achieves wide-field depth resolution with high illumination and detection efficiency.[13] Sectioning is achieved using a structured illumination technique, which has previously been demonstrated in white-light,[14] fluorescence,[15] and fluorescence lifetime[13] microscopy.

In the following sections, we discuss the design and performance of such a wide-field sectioning FLIM microscope, with particular regard to the performance of the GOI and its read-out system. The temporal resolution of the FLIM system and its ability to measure chemical and environmental changes are characterized. Practical considerations in the application of optical sectioning by structured illumination to FLIM are discussed and the sectioning strength is measured for the first time. The particular importance of charge coupled device (CCD) dynamic range to optical sectioned FLIM is highlighted and we present significantly improved performance, compared to our first proof of principle experiment, which have permitted the first artifact-free FLIM of multiple fluorophores in a single field of view.

II. FLUORESCENCE LIFETIME IMAGING MICROSCOPE

A schematic of our FLIM setup is shown in Fig. 1. Two different configurations have been used with our microscope to produce the results reported here. First, a low repetition rate laser system operating at 10 kHz was used in conjunction with a GOI, which samples the fluorescence at up to 10 kHz with a sub-100 ps minimum gate width, and, second, a high repetition rate 80 MHz commercial laser system with a high rate imager, also operating at 80 MHz and with a 200 ps minimum gate width, as the detector.

A. Excitation sources

The low repetition rate laser system consisted of a commercial Ti:sapphire laser (Spectra-Physics Tsunami), pumped by the 514.5 nm line of an argon ion laser to produce an 80 MHz laser pulse train (100 fs pulse duration, 830 nm center wavelength, and pulse energy ~10 nJ), together with a home-built Cr:LiSAF regenerative amplifier,[16] pumped by the 488 nm line of the same argon ion laser to provide ~10 μJ, 10 ps pulses at a repetition rate of up to 20 kHz. These pulses are frequency doubled to 415 nm using a β barium borate crystal, to give a pulse energy of ~1 μJ. We note that an all-solid-state diode-pumped oscillator/amplifier laser system may also be used[17] with this FLIM system. The low cost and relative portability of diode-pumped laser technology will increase the attractiveness of time-domain FLIM technology.

Then, a high repetition rate FLIM system operating at 80 MHz was used, in which the laser pulse train from the Ti:sapphire laser is directly frequency doubled to 415 nm (~190 pJ pulse energy).

B. Microscope

A home-built inverted microscope is employed in a standard epifluorescence arrangement, incorporating Olympus infinity-corrected objective lenses. The excitation light passes through a diffuser in order to uniformly illuminate the sample in the microscope. This diffuser (Edmund Scientific, transmission ⩾90%) is imaged onto the back focal plane of the objective and its divergence is selected (typically 10°) such that the excitation light is projected (after the objective lens) over an area greater than the field of view. The laser beam may be focused onto the diffuser to minimize aperturing losses at the back focal plane of the objective and the diffuser is rotated at a few hundred Hz to remove speckle caused by the spatial coherence of the laser source. For optical sectioning a metal ruled grating which is moved laterally by an actuator is placed in the conjugate plane of the sample. A dichroic beamsplitter (DCLP450, Chroma) reflects the excitation light while transmitting fluorescence above 450 nm. The fluorescence passes through an emission filter (GG430, Chroma) and a tube lens (Olympus) immediately followed by a negative focal lens, such that the effective focal length of these two lenses is 460 mm. This serves the dual purpose of increasing the image magnification of the microscope and flattening the spatial intensity distribution at the detector, although at the expense of reduced light efficiency. When light efficiency is crucial, the negative focal length lens can be removed from the system. A long-pass filter (GG430, Chroma) prevents stray excitation light from entering the detector.

C. Time gating

In the low repetition rate FLIM system, the fluorescence is incident on the wide-field time-gated optical intensifier (GOI, Kentech Instruments Ltd., ⩾ eight line pairs per millimeter spatial resolution), which consists of an 18 mm diameter S-20 photocathode and a phosphor screen sandwiching a double microchannel plate (MCP). Applying a voltage to the MCP in the range 800–1600 V varies the signal gain. The intensified image on the phosphor screen is relayed to a CCD camera by two camera lenses back to back (Nikon, fl.8, 50 mm); an inexpensive and light efficient alternative to a field lens. Wavelengths throughout the visible range may be detected by the GOI, but its sensitivity tails off above 500 nm. The spectral response of the photocathode is shown in Fig. 2. The high voltage gating pulse is applied to a mesh in front of, and capacitatively coupled to, the photocathode; the temporal response of a typical GOI pulse is given in Fig. 3. Note that it contains numerous secondary peaks, which would compromise the temporal resolution. A reverse bias voltage is therefore applied between the photocathode and the gating mesh. The voltage increases the threshold for gain and may be set such that all secondary peaks are eliminated, producing the gate width profiles seen in Figs. 4(b)–4(d). The delay between the laser pulse and the gating pulse may be changed in 25 ps steps using a mechanical delay generator (Kentech Instruments Ltd.). However, the delay that must be applied to the trigger signal from the laser oscillator is greater than the range of the delay generator and hence a

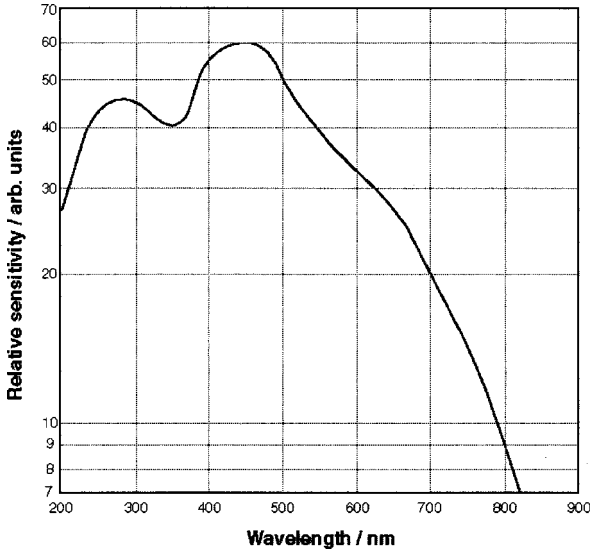

FIG. 2. Typical spectral response of an S-20 photocathode.

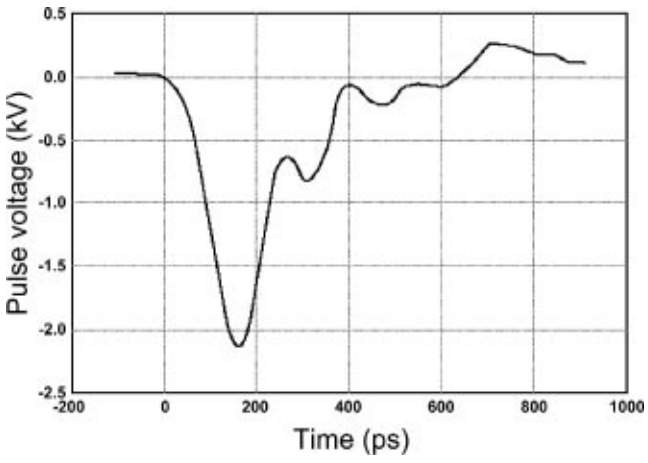

FIG. 3. Gating pulse of Kentech Instruments' GOI.

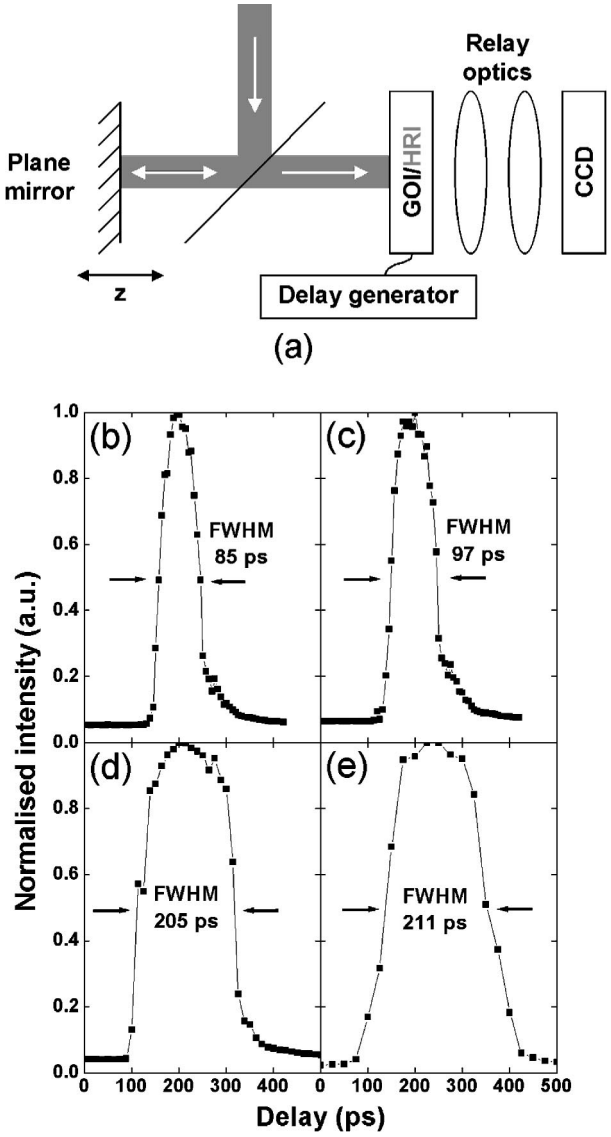

FIG. 4. Experimental determination of gate width of GOI/HRI (a) experimental setup, (b)–(e) experimental data; (b) GOI mode, <100 ps setting, (c) GOI mode, 100 ps setting, (d) GOI mode, 200 ps setting, and (e) HRI mode, 200 ps setting.

coarse electronic delay (DC 535, Stanford Research Systems) is used in addition.

With the high repetition rate FLIM system, a high rate imager (HRI, Kentech Instruments Ltd.) replaces the GOI. The principal disadvantage of the HRI compared to the GOI is that the minimum gate width is wider (200 ps for the HRI and <100 ps for the GOI) and spatial resolution is comprised. The GOI and HRI are housed within the same module and hence their spectral characteristics, for example, are identical. The gating pulse is applied directly to the photocathode in the HRI and, because the gating pulse is therefore at a lower voltage than in the GOI, proximity focusing is less and the spatial resolution is comprised. Note that the required delay between laser pulse and gating pulse in the high repetition rate is very short and hence the coarse delay is unnecessary.

The gate width of our detection system, with the intensifier in both GOI and HRI modes, was determined using the

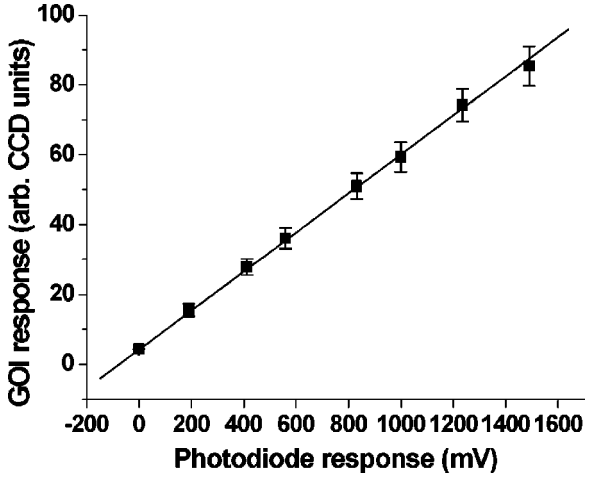

FIG. 5. Example of the response of the GOI, at a gain setting of 1200 V, to a linearly increasing signal, measured with the eight-bit camera.

simple setup shown in Fig. 4(a). A mirror was placed in the sample plane of the FLIM microscope and the dichroic beamsplitter replaced by a glass slide. The laser beam was therefore reflected, by the mirror, towards the detector; to avoid damage, the incident light was strongly attenuated with neutral density filters. Axial displacement of the mirror temporally scans the laser pulses through the gate. By measuring the signal intensity, averaged over several pixels to reduce noise, the detector gate width may thus be characterized. We assume that the laser pulse is a temporal delta function in quoting values for the gate width (the pulse duration is actually ~10 ps in the low repetition rate system with the GOI, ~100 fs in the high repetition rate system with the HRI), i.e., much shorter than the gating pulse. The time delay between the laser pulse and the gating pulse can be altered both by displacing the plane mirror and using the delay generator. Axial translation of the mirror away from the glass slide increases the delay by 6.7 ps/mm. Combining these two methods of changing the delay time, it is possible to scan rapidly through the gate width with reasonable accuracy. Figures 4(b)–4(e) shows the gate widths as measured experimentally for the GOI with set values of <100 ps, 100 ps, and 200 ps; also the HRI with a 200 ps gate width. In GOI mode, the gate widths possible range from <100 ps to 3 ns; in HRI mode, from 200 ps to 1 ns. Although a narrow gate width increases the temporal resolution, the proportion of the available fluorescence that is collected is reduced. To maximize the temporal resolution, it is clear that the shortest possible gate width for the light levels available be used. Slow decays require large gate widths to increase sensitivity.

In order to extract quantitative information from the fluorescence intensity images, it is clearly necessary for the detector to have a linear response. Figure 5 shows the response of the GOI as measured by an eight-bit intensified camera, at fixed gain, to different incident intensities. This data was obtained by using a beamsplitter to direct the laser pulses to a photodiode and the GOI simultaneously. Similarly, the response of the eight-bit camera alone to incident light was confirmed (data not shown).

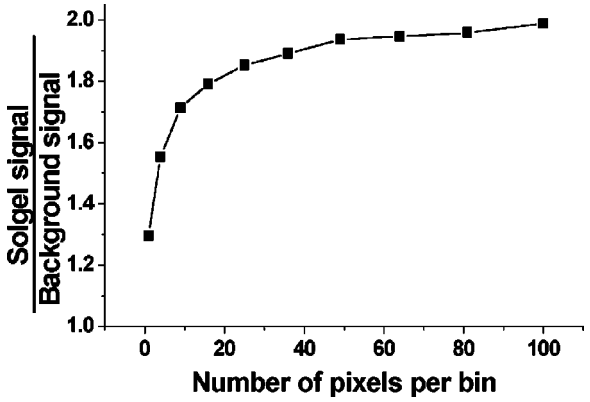

FIG. 6. Signal-to-background ratio using the 12-bit integrating camera as a function of hardware bin size. The signal-to-background ratio has been defined as the ratio between the average fluorescence intensity from a uniform sol–gel sample and the background signal (from out-of-focus light).

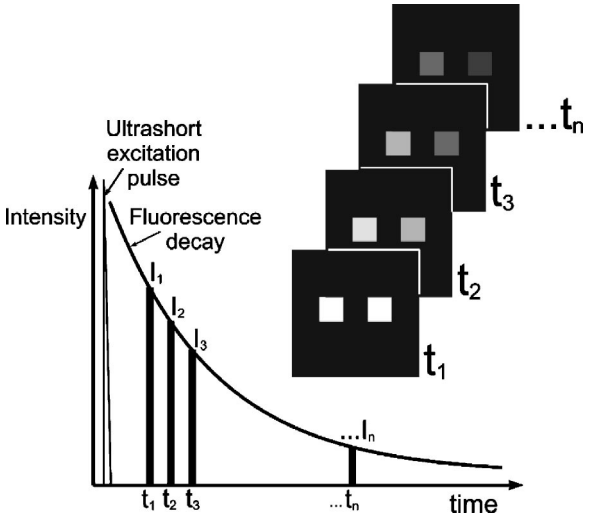

FIG. 7. A series of intensity images is acquired by sampling the fluorescence decay at a range of delays.

D. CCD detection systems

Two cameras have been used in these studies. The first is an eight-bit video rate intensified CCD camera (ISIS-III, Photonic Science, Ltd.). The intensifier and video gains may be varied between one and ten (arbitrary units). When measuring lifetimes, the camera and GOI/HRI gains are set such that the maximum intensity in the first time gate after excitation does not saturate the CCD. Because the fluorescence intensities are so low and the gains applied correspondingly high, we typically average over 20–40 frames. Images are stored as pseudo-16-bit images: averaging introduces decimal pixel information. The second CCD camera (Pentamax, Princeton Instruments) achieves enhanced sensitivity by temporal integration and has 12 bits of dynamic range. The signal-to-noise ratio for the integrating camera is superior both because the intensifier in the eight-bit camera introduces noise and because the 12-bit camera is Peltier cooled to reduce the dark current. Since the 12-bit camera CCD has a smaller active area, but the same number of pixels, one lens in the relay optics between the GOI/HRI and the CCD is replaced by a f2 35 mm lens. The integrating camera has a facility to bin pixels in hardware to enhance sensitivity at the expense of spatial resolution. Figure 6 shows the increase in contrast when pixels are binned. We used a Rhodamine 6G sol–gel block as a uniform fluorescent sample and averaged over several pixels of the sol–gel signal and the background signal (out-of-focus light), using their ratio as a measure of the signal-to-background ratio of images acquired by the camera. Note that the greatest contrast improvement is obtained when moving from a ''no binning'' setting to 2×2 binning, suggesting that this setting could be the optimum compromise between sensitivity and spatial resolution.

III. FLUORESCENCE LIFETIME IMAGING

In time-domain FLIM, the fluorescence emitted following an excitation pulse is sampled at a range of delays. In this way, the CCD, a frame grabber, and a personal computer connected to the FLIM microscope acquire a whole series of time-gated intensity images (Fig. 7). The long delay time of the phosphorescence in the GOI/HRI can cause an image to persist at the phosphor screen (P43, persistence time $\sim$300 μs). To prevent erroneously bright images, they are acquired starting with the dimmest (longest delay time) first and then moving to shorter delays. Typically, a set of images at 10–15 delay times is acquired. Using the Levenberg–Marquardt nonlinear least squares fitting algorithm, each pixel in the image set is then fitted to an exponential decay with one or two components, or to a stretched exponential decay. The lifetimes thus calculated are displayed as a lifetime map with a false color scale. The maximum lifetime that may be measured is limited solely by the repetition rate of the laser system. Longer lifetimes can be measured with the regenerative amplifier output because the pulses are temporally further apart. Although this allows increased temporal resolution of slow decays, the higher pulse energy requirement can cause photobleaching.

A. Chemically specific imaging

It was noted in the introduction that the fluorescence lifetime is dependent on both chemicals themselves and their environment. We first investigated the capability of our FLIM microscope to achieve chemically specific imaging and environmentally specific imaging using laser dyes. Figure 8(a) shows a FLIM map of five pipettes, two of the dye Coumarin 314 (80 μM in ethanol) and three containing DASPI (80 μM in a 50:50 ethanol/glycerol mixture). The mean lifetimes $\pm$ standard deviation of the two dyes were measured to be 3.46 ± 0.02 ns and 143 ± 5 ps, respectively; these values agree with independent measurements using time-correlated single photon counting and a streak camera. The high temporal dynamic range of the FLIM system is also illustrated by Fig. 8, lifetimes as short as the GOI gate width may be measured.

B. Environment specific imaging

As noted earlier, the sensitivity of the fluorescence lifetime of a fluorophore to its environment is due to the influence of the latter on the nonradiative decay rate. One environmental parameter that may be varied is the viscosity of

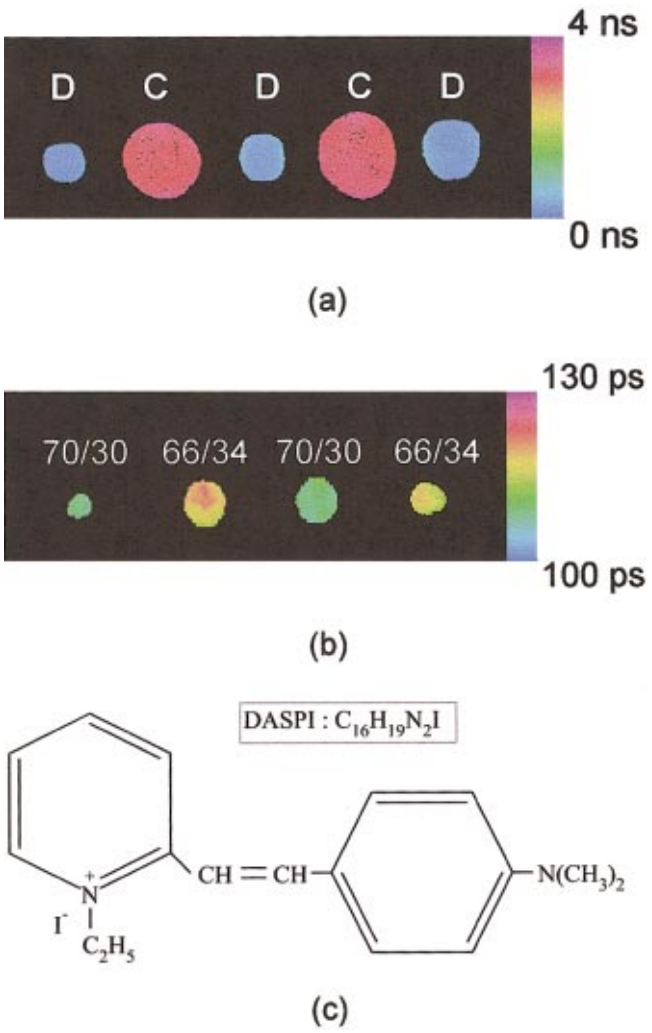

FIG. 8. (Color) (a) Chemically specific imaging is illustrated by this FLIM map of five drops of Coumarin 314 (C) and DASPI (D) solutions. The lifetime values are plotted on a false color scale. The mean lifetime ± standard deviation of the two dyes were measured to be 3.46±0.02 ns and 143±5 ps, respectively. Environment specific imaging: (b) FLIM map of two interleaved pairs of DASPI drops in solvents comprising 70% ethanol, 30% glycerol, and 66% ethanol, 34% glycerol. (c) Chemical structure of DASPI (see Ref. 26).

the solvent in which a chemical is dissolved. By dissolving DASPI in mixtures of ethanol and glycerol (viscosities 1.203 cp and 1490 cp, respectively) of different ratios (70:30 and 66:34), it was possible to show the ability of the FLIM instrument to image environmental changes. Figure 8(b) shows the fluorescence lifetime of DASPI increases with solvent viscosity. This may be explained by reference to Fig. 8(c). In structures containing two aromatic rings with an aliphatic linkage, such as DASPI, the two benzene rings can rotate with respect to the carbon chain that links them.[18] This provides a nonradiative method for the molecule to return to the ground state, thereby shortening the lifetime, but one that is impeded by increasing the viscosity because the nonradiative decay rate is lower. Note that viscosity only effects molecules with degrees of internal rotation. A more general effect, independent of molecular structure, is the lifetime dependence on the solvent refractive index. In this case, the fluorescence lifetime increases as the refractive index falls.[19] We have used the ability of our FLIM system to contrast chemical and environmental differences in imaging biological tissue *in vitro*, using autofluorescence.[20]

C. Temporal resolution and reproducibility

The temporal discrimination of the system is also illustrated by Fig. 8(b). The mean lifetimes for the 70:30 solution are 108.6±1.0 ps and 108.9±1.1 ps and for the 66:34 solution are 118.2±2.3 ps and 115.9±1.7 ps. Our FLIM microscope, therefore, has a temporal discrimination better than 10 ps. The reproducibility of lifetime measurement has been demonstrated using FLIM maps of pipettes of DASPI in four different ethanol/glycerol mixtures acquired over 100 minutes.[21] The mean lifetimes were plotted and demonstrate a reproducibility better than ±2% for the longer lifetimes and ±5% for the shortest ones, which are comparable to the gate width.

IV. OPTICAL SECTIONING BY STRUCTURED ILLUMINATION

The FLIM system uses the optical sectioning technique described in Ref. 14 and, as applied to FLIM, in Ref. 13. It is based on spatially modulated illumination, which can be achieved by imaging a grating (in the excitation path) onto the sample. If the excitation light has the sinusoidal spatial form

$$s(x,y)=1+m\cos(2\pi v x+\phi_0), \tag{1}$$

where m is the modulation depth, v is the spatial frequency, and ϕ_0 is an arbitrary spatial phase, then the resulting fluorescence image will have the form

$$I(x,y)=I_c+I_s\cos(2\pi v x+\phi_0). \tag{2}$$

The first term in Eq. (2) is the dc component, which only attenuates weakly with defocus, while the second term carries the modulation information. Because the grating is only imaged efficiently on to the part of the sample which is in focus, I_s is the image of a thin optical section and I_c is the conventional image that would be obtained without optical sectioning. To extract I_s and I_c from measured intensities, it is necessary to acquire three images I_1, I_2, and I_3 at relative spatial phases 0, $2\pi/3$ and $4\pi/3$ and use[14]

$$I_s=\frac{3}{\sqrt{2}}[(I_1-I_2)^2+(I_1-I_3)^2+(I_2-I_3)^2]^{1/2}, \tag{3}$$

$$I_c=\frac{(I_1+I_2+I_3)}{3}. \tag{4}$$

Although a sinusoidal grating will therefore, in principle, give optimal sectioning, square gratings are more light efficient because the amplitude of the fundamental harmonic is 14% greater. Provided that the mark-space ratio of the grating is one, the transmission is a sum of odd order harmonics only. By acquiring images at three spatial positions, the third order is mathematically eliminated in Eq. (3), while higher orders are sufficiently attenuated by the optical transfer function of the microscope that they may be ignored. A square

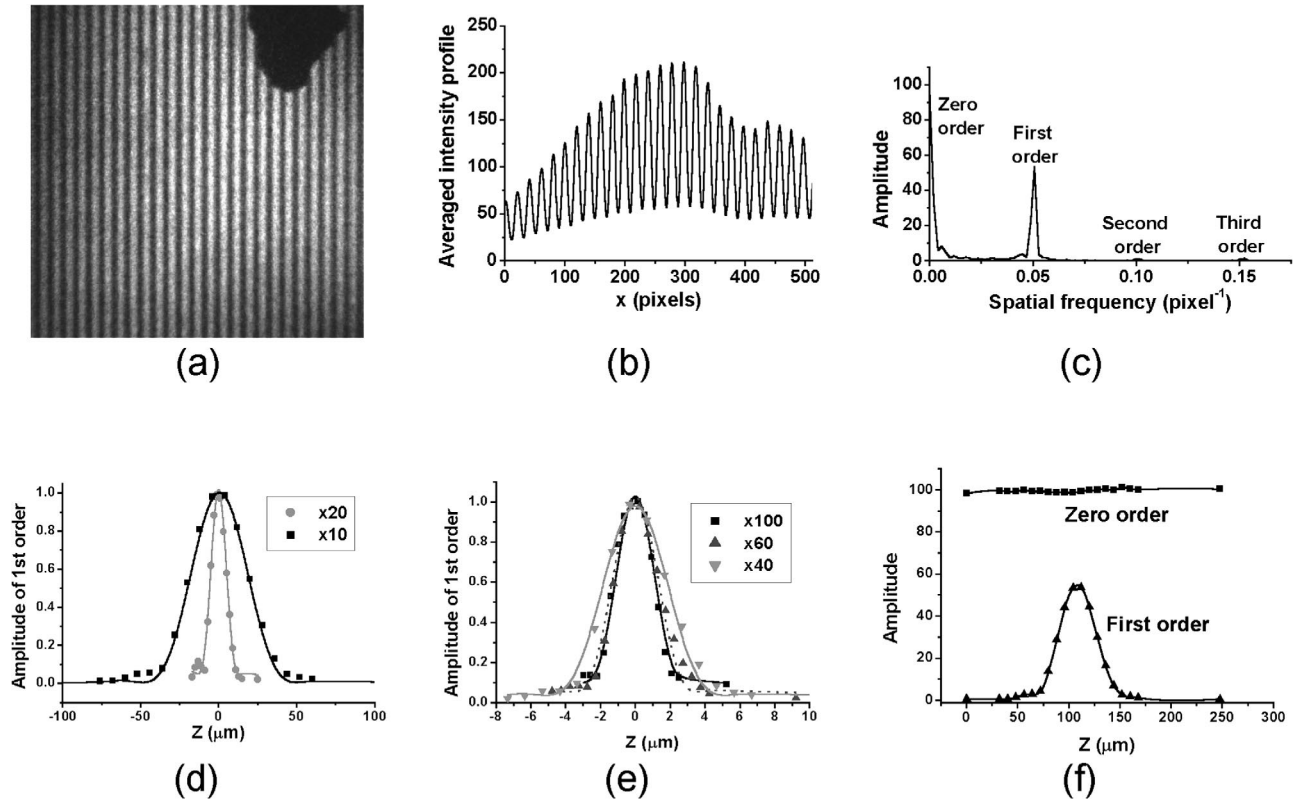

FIG. 9. Determination of the sectioning strength of the FLIM microscope. (a) Fluorescence intensity image of a thin layer from a marker pen on a glass slide, showing the modulation caused by the grating projection. (b) Each pixel column from (a) was averaged to produce the cross section through the image shown. (c) Fourier transform of (b), indicating the various orders. (d) Axial response for ×10 and ×20 objectives, with curve fits using Eq. (5) as if v_n and u were unknown. (e) Axial response for ×40, ×60, and ×100 objectives, with curve fits using Eq. (5) as if v_n and u were unknown. (f) Amplitudes of the zero and first orders for ×10 objective, thus comparing the intrinsic sectioning strength of the objective with the structure illumination technique.

wave grating is therefore a higher transmission equivalent to a sinusoidal grating for the purposes of this optical sectioning method.

There are several reasons why the sectioned image may retain a residual grating structure, which we have described in detail.[22] We have identified three factors which, when corrected for, remove the grating pattern. If the average intensity or the lateral intensity distribution varies between the three images, the images must be normalized (uniform and field normalization respectively). Additionally, the relative phase of each of the three images must be adjusted if the grating is not moved the correct distance.

The sectioning strength (axial response) of the microscope is the axial distance between the two points at which the intensity of the sectioned image has half the value of that when the grating is in focus. The normalized axial intensity response $I_p(z)$ and the normalized spatial frequency v_n are given by[23]

$$I_p(z)=\left|\frac{2J_1[uv_n(1-v_n/2)]}{[uv_n(1-v_n/2)]}\right|^2, \tag{5}$$

$$v_n=\frac{f_g\lambda M v}{(NA)f_t}, \tag{6}$$

where

$$u=\left(\frac{8\pi}{\lambda}\right)zn\sin^2\left(\sin^{-1}\frac{(NA)}{n}/2\right), \tag{7}$$

and where λ is the excitation wavelength, z is the axial position, n is the refractive index of the immersion medium, f_g and f_t are the focal lengths of the lenses imaging the grating onto the sample and the tube lens (*not* the *effective* tube lens), respectively, *NA* and *M* are the numerical aperture and magnification of the objective, respectively, v is the spatial frequency of the grating, and J_1 is the first order Bessel function.

To measure the sectioning strength requires a laterally homogeneous fluorescent object whose thickness is smaller than the axial response. We used a thin layer of fluorescent marker pen on a glass slide, with a cover slip over as the objectives used were cover slip corrected, with the high repetition rate FLIM system. One method of measuring the sectioning strength of the microscope is to acquire images of the test object at three lateral grating positions for a range of axial values and calculate the sectioned images in the usual way. The full width at half maximum of a graph of the mean intensities of these sectioned images against axial position is the sectioning strength. A similar procedure with the conventional images gives the intrinsic axial response of the objective used. A simpler and equivalent method is to measure the modulation depth when a thin test object is moved through focus. By acquiring an image with structured illumination [Fig. 9(a)] and averaging all columns of pixels, we obtain the intensity profile shown in Fig. 9(b). Note that although the grating imaged onto the sample has the form of a square

TABLE I. Theoretical, calculated using Eq. (5), and measured sectioning strengths of the FLIM microscope for a range of Olympus objectives. In each case, the grating pitch was 8 lines per millimeter, the focal lengths of the tube lens and the lens imaging the grating onto the sample were 180 mm and 150 mm, respectively, and the excitation wavelength was 415 nm.

Objective magnification	Numerical aperture	Refractive index	Theoretical sectioning strength (μm)	Measured sectioning strength (μm)
X10	0.25	1.00	32.2	41.6
X20	0.4	1.00	9.93	11.5
X40	0.65	1.00	2.86	4.32
X60	0.8	1.00	1.44	3.04
X100	1.25	1.55	0.856	2.78

wave, the fluorescence imaged onto the CCD has an approximately sinusoidal form. This is due to scattering of both excitation and emission light within the sample and rejection of higher order frequencies on each light passage of the objective and the HRI(/GOI). The modulation depth is greatest when the grating and the fluorescent layer are in conjugate planes of the microscope. By performing a Fourier transform [Fig. 9(c)], the dc background and the modulation can be separated. The amplitudes of the zero and first orders of the Fourier transform in Fig. 9(c) are equivalent to the intensities of the conventional and sectioned images, respectively. This is because the first order is the frequency of the bar grating. The weak second order is attributed to an unequal mark/space ratio for the grating being used. The tiny amplitude of the third order demonstrates that the optical transfer function of the microscope allows only weak transmission of higher harmonic spatial frequencies. From Eqs. (5) and (6), the sectioning strength of the microscope depends on the spatial frequency of the modulation at the sample and the objective used. Figures 9(d) and 9(e) show the measured sectioned image intensity as a function of axial sample position (defocus) for a range of objectives, with curve fits using Eq. (5) as if v_n and u were unknown. Note that the $\times 100$ objective is for oil immersion use and therefore a different refractive index (1.55 rather than 1.0) had to be used when calculating the spatial frequency of the modulation on the sample. Figure 9(f) compares, for a $\times 10$ objective, the inherent axial response of the conventional FLIM microscope with that of our structured illumination technique. This demonstrates the importance of optical sectioning by structured illumination in the removal of out-of-focus light. The measured sectioning strengths are compared to their theoretical value, calculated using Eq. (5), in Table I. We attribute the discrepancy between the measured and theoretical values to the assumption of Eq. (5) that the fluorescence wavelength is equal to that of the excitation and that no coverslip is present. In addition, the increased refractive index of immersion oil increases the depth of focus of the $\times 100$ objective. In principle, using a high spatial frequency grating could increase the sectioning strength. Indeed in standard fluorescence microscopy, where the CCD determines the spatial frequencies that may be resolved, smaller grating pitches have been used. In our system, however, the HRI/GOI acts as a low pass filter and the minimum resolvable grating period at the detector is limited to 80 μm at best, which is when the gate is at the widest setting.

When calculating the sectioned image, it should be noted that Eq. (3) involves the difference between images. This makes it vulnerable to the relative noise level and the dynamic range of the camera. FLIM maps of fluorescent microspheres (Molecular Probes "fluospheres," blue green and green yellow of 15 μm and 4.5 μm diameter, respectively) were produced from data acquired using the high repetition rate system by the eight-bit camera described; they are shown in Fig. 10. We used a $\times 100$ immersion oil objective with 1.25 *NA*, a 50 line pairs per inch grating and a tube lens focal length of 18 cm ($v_n = 0.055$, theoretical sectioning strength 3.18 μm). The pixels were binned in software in order to improve the signal-to-background ratio (as discussed in Fig. 6); each 2×2 pixel region in the intensity images became a single super pixel in the FLIM map. The grating was imaged onto two planes separated by 6.4 μm such that mainly only the large microspheres appear in both optical sections. Immersion oil surrounded the microspheres to ensure index matching. In the first plane of Fig. 10 (left-hand side column), the microspheres are better resolved in the sectioned intensity image [Fig. 10(c)] than the conventional image [Fig. 10(a)] because out of focus blur has been removed, thus enhancing contrast. In the second plane [Fig. 10(b)], the blur due to the small microspheres has been relatively successfully removed and the large microspheres are only resolvable on sectioning [Fig. 10(d)]. In both planes, optical sectioning has improved spatial resolution in the intensity images by removing out of focus blur. In the conventional FLIM maps [Figs. 10(e) and 10(f)], the two different microsphere types are clearly contrasted in lifetime, although with incorrect lifetime values as is shown later, but the small microspheres cannot be spatially resolved. In the sectioned FLIM map, the two microsphere types are clearly contrasted spatially due to improved spatial resolution, but are barely distinguishable by their lifetimes, and they appear speckled. The latter is indicative of a broad distribution of lifetimes being calculated for a single fluorophore, as is clearly shown in Figs. 12(a) and 12(b). The broad distribution is not real, but an artifact due to the low signal-to-noise ratio, yielding different lifetimes for different pixels of the same fluorophore. This is demonstrated by Fig. 11, where we have removed the artifact by increasing the dynamic range of the CCD. We have used the 12-bit camera described in a system which has an effective focal length of 46 cm and hence a $\times 40$ objective with 0.65 NA and 8 lines/mm grating to ensure a similar field of view and spatial frequency ($v_n = 0.17$,

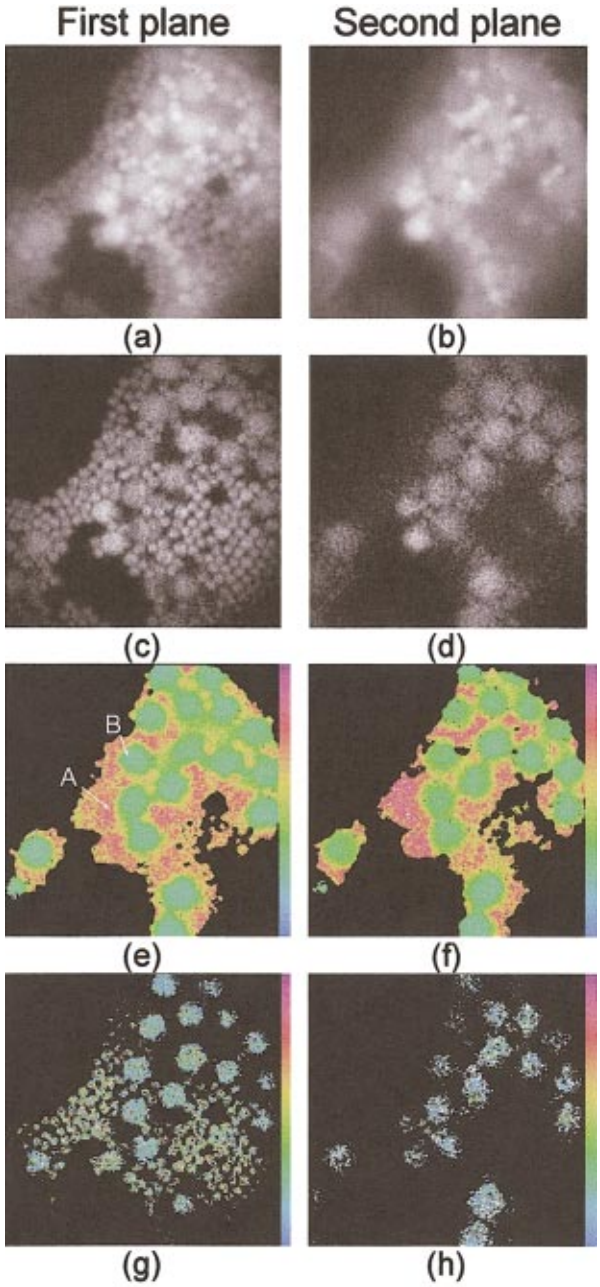

FIG. 10. (Color) Conventional gated fluorescence intensity images (a), (b); sectioned gated fluorescence intensity images (c), (d); conventional FLIM maps (e), (f); sectioned FLIM maps (g), (h) of two planes 6.4 μm axially apart containing 4.5 μm and 15 μm diameter microspheres, acquired using an eight-bit camera in the high repetition rate system. All FLIM maps are scaled to a lifetime range of 1500(blue)–7000 ps. A $\times$100 immersion oil objective was used and immersion oil filled the space between microsphere layers. The grating had a pitch of 50 lines per inch and the images were binned 2$\times$2 in software. For each grating position, 20 images acquired at video rate were averaged.

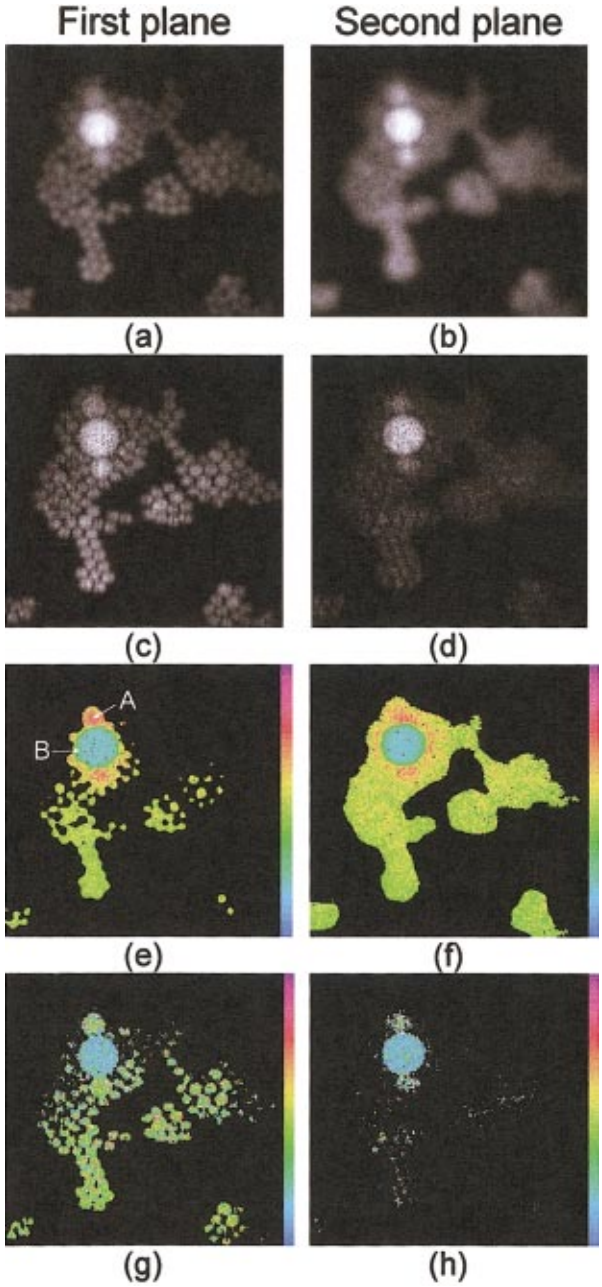

FIG. 11. (Color) Conventional gated fluorescence intensity images (a), (b); sectioned gated fluorescence intensity images (c), (d); conventional FLIM maps (e), (f); sectioned FLIM maps (g), (h) of two microsphere-containing planes 4 μm apart, acquired using a 12-bit camera in a high repetition rate system. All FLIM maps are scaled to 1500(blue)–7000 ps. A $\times$40 objective was used and immersion oil filled the space between microsphere layers. The grating had a pitch of eight lines per millimeter and the images were binned 2$\times$2 in hardware. Image acquisition time was 1 s and no averaging was used. (The intermediate size beads of approximately 10 μm diameter immediately above and below the large bead are rogue microspheres with the same fluorescence characteristics as those of 4.5 μm diameter.)

theoretical setting strength 4.32 μm) at the HRI. (The sectioning strength is dependent only on the modulation frequency at the sample, rather than at the HRI; however, the grating chosen must be resolvable by the HRI.) In Fig. 11, the quality of the conventional [Figs. 11(a) and 11(b)] and sectioned [Figs. 11(c) and 11(d)] *intensity* images is broadly the same as in Fig. 10. Again, the conventional FLIM maps [Figs. 11(e) and 11(f)] display a range of lifetimes for each microsphere type, which, furthermore, are not equal to the lifetimes in the sectioned FLIM maps [Figs. 11(g) and 11(h)]. However, the lifetime distributions of each microsphere type are much narrower [Figs. 12(c) and 12(d)] indicating an improved signal-to-noise ratio and enhanced spatial resolution.

In the conventional image, at the point marked "A" in Figs. 10(e) and 11(e), there is a lifetime artifact that we ex-

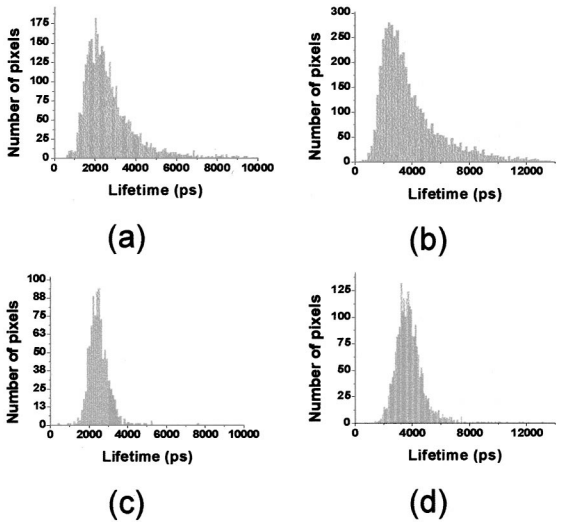

FIG. 12. Lifetime distributions for 15 μm blue (a), (c) and 4.5 μm green (b), (d) microspheres acquired with eight-bit camera (a), (b) and 12-bit camera (c), (d), calculated from Figs. 10(g) and 11(g), respectively.

plain in the following way. Because the large microspheres emit at a wavelength that excites the small microspheres more efficiently than the laser excitation, this causes an initial increase in the fluorescence intensity before the usual exponential decay profile.[24] When a single exponential model is inappropriately fitted to such a decay profile, the lifetime calculated is greater than those of either microsphere. The sectioned image, however, only contains information from spatially *modulated* fluorescence and therefore only includes fluorescence *directly* excited by the modulated laser light. The intensity of a pixel is a sum of the contributions of all the fluorophores within the point spread function (PSF) of the optical system.[25] Because the PSF is broader for the conventional image, there is an additional out-of-focus component at ''B'' [in Figs. 10(e) and 11(e)] from the small microspheres that is not present in the sectioned image. A single exponential model is also inappropriate for two different fluorophores and this manifests itself as a range of different lifetimes that fall between, and depend on the relative amplitude of, the two components. We assume that this affects the small microspheres as well, but that it cannot be separated from the dominant effect of indirect excitation by the large microspheres. Optical sectioning is therefore necessary in order to remove lifetime artifacts, for which the structured illumination technique is shown here to be capable. In principle, the best sectioned image will be obtained using a camera with the greatest bit depth. Because greater signal strengths are needed to fully utilize the effective dynamic range of such cameras (as commercially available), it is necessary to apply higher gain in the GOI/HRI. Image intensification degrades the signal-to-noise ratio and so a balance must be found between image improvement by reduced gain and increased camera bit depth. With optical sectioning, a high quality FLIM image demands a greater signal-to-noise ratio than a fluorescence intensity image does. This will make high signal-to-noise ratios imperative when applying the technique in the future to biological tissue. Scattering will degrade image quality in both the lateral and axial spatial dimensions.

ACKNOWLEDGMENTS

Funding for this research from the UK Engineering and Physical Sciences Research Council (EPSRC), the Biotechnical and Biological Sciences Research Council (BBSRC), and the Paul Instrument Fund of the Royal Society is gratefully acknowledged. Two of the authors (M. J. C. and K. D.) acknowledge EPSRC CASE studentships with the Institute of Cancer Research at the ICR/Royal Marsden National Hospital trust. One of the authors (S. E. D. W.) acknowledges an EPSRC studentship.

[1] J. R. Lakowicz, *Principles of Fluorescence Spectroscopy* (Kluwer, New York, 1999).
[2] R. Sanders, A. Draaijer, H. C. Gerritsen, P. M. Houpt, and Y. K. Levine, Anal. Biochem. **227**, 302 (1995).
[3] J. R. Lakowicz, H. Szmacinski, and M. L. Johnson, J. Fluoresc. **2**, 47 (1992).
[4] K. Dowling, M. J. Dayel, M. J. Lever, P. M. W. French, J. D. Hares, and A. K. L. Dymoke-Bradshaw, Opt. Lett. **23**, 810 (1998).
[5] R. Cubeddu, A. Pifferi, P. Taroni, A. Torricelli, G. Valentini, F. Rinaldi, and E. Sorbellini, IEEE J. Sel. Top. Quantum Electron. **5**, 923 (1999).
[6] P. C. Schneider and R. M. Clegg, Rev. Sci. Instrum. **68**, 4107 (1997).
[7] K. C. Benny Lee, J. Siegel, S. E. D. Webb, S. Lévêque-Fort, M. J. Cole, R. Jones, K. Dowling, P. M. W. French, and M. J. Lever, Biophys. J. **81**, 1265 (2001).
[8] G. Weber, J. Phys. Chem. **85**, 949 (1981).
[9] A. Squire, P. J. Verveer, and P. I. H. Bastiaens, J. Microsc. **197**, 136 (2000).
[10] K. Carlsson and A. Liljeborg, J. Microsc. **191**, 119 (1998).
[11] J. Systma, J. M. Vroom, C. J. De Grauw, and H. C. Gerritsen, J. Microsc. **191**, 39 (1998).
[12] M. Straub and S. W. Hell, Appl. Phys. Lett. **73**, 1769 (1998).
[13] M. J. Cole, J. Siegel, S. E. D. Webb, R. Jones, P. M. W. French, M. J. Lever, L. O. Sucharov, M. A. A. Neil, R. Juškaitis, and T. Wilson, Opt. Lett. **25**, 1361 (2000).
[14] M. A. A. Neil, R. Juškaitis, and T. Wilson, Opt. Lett. **22**, 1905 (1997).
[15] M. A. A. Neil, A. Squire, R. Juškaitis, P. I. H. Bastiaens, and T. Wilson, J. Microsc. **197**, 1 (2000).
[16] S. C. W. Hyde, N. P. Barry, R. Mellish, P. M. W. French, J. R. Taylor, C. J. van der Poel, and A. Valster, Opt. Lett. **20**, 160 (1995).
[17] R. Mellish, N. P. Barry, S. C. W. Hyde, R. Jones, P. M. W. French, J. R. Taylor, C. J. Van der Poel, and A. Valster, Opt. Lett. **20**, 2312 (1995).
[18] J. R. Taylor, M. C. Adams, and W. Sibbett, Appl. Phys. **21**, 21 (1980).
[19] K. Suhling, D. M. Davis, Z. Petrásek, J. Siegel, and D. Phillips, Proc. SPIE **4259**, 92 (2001).
[20] R. Jones, K. Dowling, M. J. Cole, D. Parsons-Karavassilis, M. J. Lever, P. M. W. French, J. D. Hares, and A. K. L. Dymoke-Bradshaw, Electron. Lett. **35**, 256 (1999).
[21] K. Dowling, M. J. Dayel, S. C. W. Hyde, P. M. W. French, M. J. Lever, J. D. Hares, and A. K. L. Dymoke-Bradshaw, J. Mod. Opt. **46**, 199 (1999).
[22] M. J. Cole, J. Siegel, S. E. D. Webb, R. Jones, K. Dowling, M. J. Dayel, D. Parsons-Karavassilis, P. M. W. French, M. J. Lever, L. O. D. Sucharov, M. A. A. Neil, R. Juškaitis, and T. Wilson, J. Microsc. **203**, 246 (2001).
[23] T. Wilson and D. Karadaglić, Proceedings of the Inter-Institute Workshop on *In Vivo* Optical Imaging at the NIH, Washington, 1999, p. 7.
[24] J. Siegel, D. S. Elson, S. E. D. Webb, D. Parsons-Karavassilis, S. Lévêque-Fort, M. J. Cole;, M. J. Lever, P. M. W. French, M. A. A. Neil, R. Juškaitis, L. O. Sucharov, and T. Wilson, Opt. Lett. **26**, 1338 (2001).
[25] A. Squire and P. I. H. Bastiaens, J. Microsc. **193**, 36 (1999).
[26] U. Brackman, *Lamdachrome Laser Dyes* (Lambda Physik Gmbh, Göttingen, 1986).